Single-Shot Intensity- and Phase-Sensitive Compressive Sensing-Based Coherent Modulation Ultrafast Imaging

Chengzhi Jin[1,*], Yingming Xu,[2,3,*] Dalong Qi[1,†], Yunhua Yao,[1] Yuecheng Shen[1], Lianzhong Deng,[1] Ruozhong Han,[1] Zhen Pan,[1] Jiali Yao,[1] Yilin He,[1] Zhengqi Huang,[1] Xingchen Pan[2], Hua Tao,[2] Mingying Sun[2], Cheng Liu,[2] Junhui Shi,[3] Jinyang Liang,[4] Zhiyong Wang,[5] Jianqiang Zhu,[2,‡] Zhenrong Sun,[1] and Shian Zhang[1,6,7,§]

[1]*State Key Laboratory of Precision Spectroscopy, School of Physics and Electronic Science, East China Normal University, Shanghai 200241, China*
[2]*Key Laboratory of High Power Laser and Physics, Shanghai Institute of Optics and Fine Mechanics, Chinese Academy of Sciences, Shanghai 201800, China*
[3]*Research Center for Humanoid Sensing, Zhejiang Lab, Hangzhou 311100, China*
[4]*Laboratory of Applied Computational Imaging, Centre Énergie Matériaux Télécommunications, Institut National de la Recherche Scientifique, Varennes, Québec J3X1S2, Canada*
[5]*School of Mathematical Sciences, University of Electronic Science and Technology of China, Chengdu 611731, China*
[6]*Collaborative Innovation Center of Extreme Optics, Shanxi University, Taiyuan 030006, China*
[7]*Joint Research Center of Light Manipulation Science and Photonic Integrated Chip of East China Normal University and Shandong Normal University, East China Normal University, Shanghai 200241, China*

Ultrafast imaging can capture the dynamic scenes with a nanosecond and even femtosecond temporal resolution. Complementarily, phase imaging can provide the morphology, refractive index, or thickness information that intensity imaging cannot represent. Therefore, it is important to realize the simultaneous ultrafast intensity and phase imaging for achieving as much information as possible in the detection of ultrafast dynamic scenes. Here, we report a single-shot intensity- and phase-sensitive compressive sensing-based coherent modulation ultrafast imaging technique, shortened as CS-CMUI, which integrates coherent modulation imaging, compressive imaging, and streak imaging. We theoretically demonstrate through numerical simulations that CS-CMUI can obtain both the intensity and phase information of the dynamic scenes with ultrahigh fidelity. Furthermore, we experimentally build a CS-CMUI system and successfully measure the intensity and phase evolution of a multimode Q-switched laser pulse and the dynamical behavior of laser ablation on an indium tin oxide thin film. It is anticipated that CS-CMUI enables a profound comprehension of ultrafast phenomena and promotes the advancement of various practical applications, which will have substantial impact on fundamental and applied sciences.

Ultrafast optical imaging (UOI) [1–3] can record the dynamic scenes with a nanosecond and even femtosecond temporal resolution, and therefore it plays an irreplaceable role in the visualization and analysis of ultrafast phenomena. So far, UOI has been widely used in various fields, such as materials science [4,5], biomedicine [6], physics [7], and chemistry [8]. However, most UOI techniques are unable to retrieve the phase information based on the pure intensity measurements, which greatly limits the integrity of the detected information. In general, phase imaging can provide the information about the object's morphology, refractive index, thickness, or other information that intensity imaging cannot offer, which plays a very important role in analyzing and understanding the ultrafast dynamic behavior [9,10]. Therefore, it is important to realize the simultaneous ultrafast intensity and phase imaging for achieving as much information as possible in the detection of ultrafast dynamic scenes. Recently, single-shot ultrafast complex amplitude

imaging techniques have made significant progress, which enable the multiframe simultaneous perception of intensity and phase information by combining phase-computed imaging techniques with a series of ultrafast imaging methods. For instance, Moon *et al.* [11] reported a single-shot ultrafast holographic microscopy using time and spatial frequency multiplexing. Tang *et al.* [12] demonstrated a compressed optical field topography by integrating the coded aperture snapshot spectral imaging with a global 3D phase retrieval procedure. Hu *et al.* [13] introduced a single-shot ultrafast phase retrieval technique that combines multiangle illumination and coherent diffraction imaging (CDI). Xu *et al.* [14] presented a type of single-shot ultrafast multiplexed CDI technique, which applies a multiplexed strategy with time-delayed burst illumination. Unfortunately, these ultrafast complex amplitude imaging techniques by directly combining traditional ultrafast imaging with conventional phase imaging still face great challenges, because the intricate

optical paths often introduce systematic errors, and the nested algorithm designs do not guarantee computational convergence.

To overcome these limitations mentioned above, here we develop a single-shot intensity- and phase-sensitive compressive sensing-based coherent modulation ultrafast imaging (i.e., CS-CMUI) technique that introduces the compressive sensing theory [15] and time-deflected imaging technique [16] into coherent modulation imaging [17]. CS-CMUI uses a streak camera with a fully open entrance port to compressively capture a dynamic scene after coherent diffraction and phase modulation, and then employs an iterative algorithm combining the plug-and-play (PnP) [18] framework and deep image prior (DIP) [19] (i.e., PnP-DIP) to quantitatively reconstruct the intensity and phase data of the original dynamic scene from the compressed image. Through the numerical simulation of CS-CMUI with complex amplitude data, the recovered results exhibit significantly superior quality evaluated by various image quality assessment methods when compared to the original images, which mathematically confirm the measurement precision of CS-CMUI. Subsequently, the spatiotemporal intensity and phase distribution of a Q-switched nanosecond laser pulse and the laser ablation dynamics on an indium tin oxide (ITO) thin film are experimentally measured by CS-CMUI. These measured results agree with the previous experimental observations, which demonstrate the experimental feasibility of CS-CMUI.

The CS-CMUI involves two main steps: data compression acquisition and algorithmic image reconstruction. The data acquisition process is illustrated in Fig. 1(a), where the dynamic scene carrying the intensity and phase information undergoes spatial diffraction, followed by compression and recording after random phase modulation, spatiotemporal deflection, and intensity integration. All the above processes can be expressed in a form of matrix as

$$E(x', y') = \mathbf{TS}|\mathbf{H}_{z_2}\mathbf{MH}_{z_1}U(x, y, t)|^2, \quad (1)$$
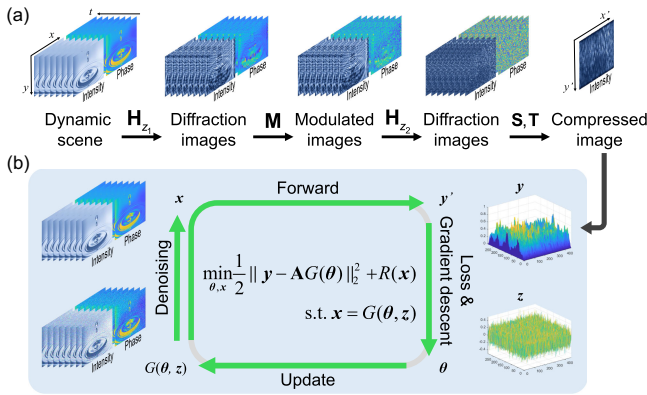

FIG. 1.   The data flowchart of CS-CMUI. (a) Data acquisition diagram of CS-CMUI. (b) Data flowchart of CS-CMUI image reconstruction.

where $E(x', y')$ is the measured intensity snapshot, $U(x, y, t)$ is the complex amplitude information of original dynamic scene, and $\mathbf{H}_{z_1}$ and $\mathbf{H}_{z_2}$ are the spatial propagation operators with different distances, $\mathbf{M}$ represents the phase modulation operator, $\mathbf{S}$ represents the spatiotemporal deflection operator of the streak camera, $\mathbf{T}$ represents the integration operator of CMOS in the streak camera. The recorded snapshot is then utilized to recover the original dynamic scene via a PnP-DIP algorithm. For simplicity, we use x to represent the complex amplitude distribution of the dynamic scene under measurement, $\mathbf{A}$ to denote the measurement matrix of the entire system, and y to represent the final compressed data. Thus, the inverse problem can be regarded as an optimization problem in the following form by introducing DIP instead of the inverse operator, and is written as [20]

$$\min_{\boldsymbol{\theta}, x} \frac{1}{2} \|y - \mathbf{A}G(\boldsymbol{\theta}, z)\|_2^2 + \lambda R(x) \text{ s.t.} \quad x = G(\boldsymbol{\theta}, z), \quad (2)$$

where $\|y - \mathbf{A}G(\boldsymbol{\theta}, z)\|_2^2$ is a fidelity term, which refers to the degree of agreement between the reconstructed image and the acquired data, $\| \bullet \|_2$ denotes the l_2 norm, $R(x)$ is a prior term, also known as the regularization term or penalty term, which incorporates prior knowledge or assumptions about the original image characteristics, and λ is a regularization parameter to balance the fidelity term and the prior term. $G(\boldsymbol{\theta}, z)$ represents a deep convolutional neural network with updatable parameters, its input z is a standard Gaussian-distributed white noise with the same size as the original data x, and $\boldsymbol{\theta}$ is an updatable weight parameter in the network. The entire image reconstruction process is shown in Fig. 1(b). After a finite number of iterations, the 3D time-resolved complex amplitude information x, restoring the original dynamic scene, can be accurately reconstructed by applying the alternating direction method of multipliers algorithm [21]. In this framework, the optimization problem with constraint is decomposed into three subproblems of images denoising, first-order gradient backward descent, and residual accumulation. After the image reconstruction, the spatiotemporal intensity and phase evolutions of the dynamic scene can be successfully obtained. Please refer to Supplemental Material, Note 1 [22] for more details on the mathematical principles.

To better illustrate the technical performance and application potential of CS-CMUI, a motion scene containing four frames of complex amplitude light field is simulated, which consists of four intensity distribution images and four phase distribution images. The original intensity and phase images as ground truths are shown in the top patterns of Figs. 2(a) and 2(b), respectively. After the data acquisition, a 2D compressed snapshot can be obtained from the simulation, as shown in Fig. 2(c). The specific details are provided in Supplemental Material, Note 2 [22]. It is worth noting that CS-CMUI in this case does not require the
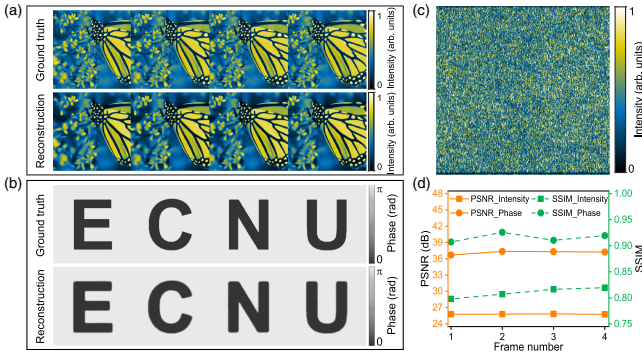
FIG. 2. The simulation of CS-CMUI. (a) Ground truths and reconstructed intensity images, which consist of four butterfly images parallel moving in the horizontal direction. (b) Ground truths and reconstructed phase images, which consist of four changing letters of E, C, N, and U. (c) Compressed snapshot collected through CS-CMUI's forward transmission. (d) PSNR (orange line) and SSIM (green line) values calculated by the reconstructed intensity and phase images compared with ground truths.
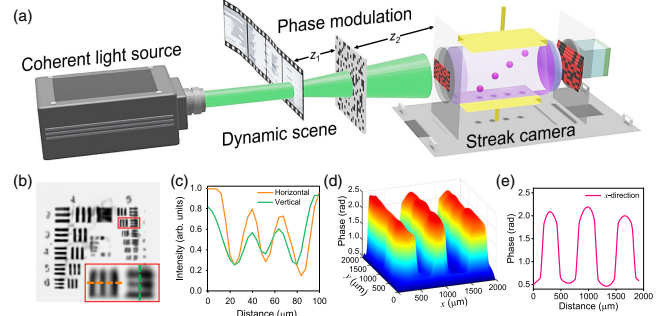

FIG. 3. Experimental setup and system characterization. (a) System configuration of CS-CMUI. (b) Calibration of static spatial resolution. The subimage at the bottom right corner is the enlarged area in the red box. (c) Intensity variations along the orange (vertical strips) and green (horizontal strips) dashed lines in (b). (d) Test of the capability for dynamic phase quantitative detection. (e) Average phase variation along the x direction in (d).

constraint of polygonal apertures in front of the object plane due to the introduction of compressive sensing, which still enables signal recovery below the Nyquist sampling rate, and so the complete field of view can be obtained. Furthermore, the intensity and phase images reconstructed via the PnP-DIP algorithm are shown in the bottom patterns of Figs. 2(a) and 2(b), respectively. To objectively assess the image reconstruction quality, a peak signal-to-noise ratio (PSNR) and a structural index similarity (SSIM) between the recovered results and the original data are calculated one by one, and the calculation results are presented in Fig. 2(d). The average PSNR of the recovered phase results is 37.15 dB, and the average SSIM is 0.9157. The average PSNR of the recovered intensity results is 25.79 dB, and the average SSIM is 0.8103. These simulation results indicate that CS-CMUI can obtain the original complex amplitude information of the dynamic scene with very high fidelity.

The experimental setup of CS-CMUI is shown in Fig. 3(a), which mainly includes a coherent light source, a dynamic scene, a phase modulation plate, and a streak camera. A laser pulse from the coherent light source (CNI, DPS-532-A) is used as illumination to irradiate the dynamic scene with a time-varying intensity and phase. The illumination laser pulse is modulated by the dynamic scene, and therefore the transmitted laser pulse carries the intensity and phase information of the dynamic scene. After propagating a distance of $z_1 = 70$ mm and reaching the phase modulation plate (50 μm × 50 μm elements, π modulation, a simulation result assessing the impact of the modulation regimes on the reconstruction quality is provided in Supplemental Material, Note 3 [22]), the transmitted laser pulse undergoes random phase modulation, and then further propagates another distance of

$z_2 = 30$ mm before irradiating the photocathode of the streak camera (Hamamatsu, C7700). Then, the streak camera translates the temporal information of the dynamic scene into the differences in the spatial position. Finally, the transmitted laser pulse is captured as a compressed intensity snapshot by the CMOS camera. Furthermore, to calibrate the spatial resolution and quantify the phase detection capabilities of CS-CMUI, a 1951 USAF resolution test target and a multistriped glass step target with an identical height are positioned in the object plane for measurement, and the experimental results are shown in Figs. 3(b)–3(e). The static spatial resolution and the average phase error of CS-CMUI can be determined to be approximately 13.92 μm and 0.057 radians, respectively. The particulars of the experimental setup and the system characterization are described in Supplemental Material, Note 4 [22].

To experimentally verify the single-shot intensity and phase detection capability of CS-CMUI, an "E"-shaped modulated nanosecond laser pulse is first measured, the schematic diagram as shown in Fig. 4(a), and further elaboration of this experiment can be found in Supplemental Material, Note 5 [22]. 21 intensity and 21 phase images with a 1 ns frame interval are recovered, and only six intensity and six phase images from −5 to 5 ns with a 2 ns frame interval are shown as a representative in Figs. 4(b) and 4(c), respectively. Here, the time zero is set as the moment corresponding to the maximum laser pulse intensity. The complete sequence is available in Supplemental Material, Movie 1 [36].

As shown in Fig. 4(b), the intensity images of the letter E reveal a spatial movement from the lower-left to the upper-right corner, which is caused by the multimode output and mode competition of the laser pulse [37]. The spatial intensity in each intensity image is integrated, and the outcomes are presented in Fig. 4(d). For comparison, the laser pulse intensity evolution is measured using the streak
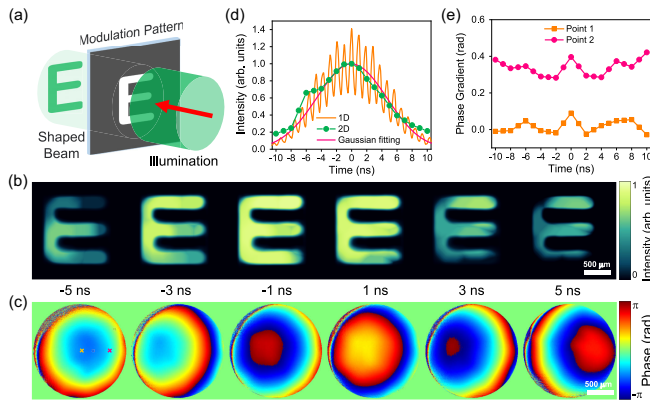
FIG. 4. Optical field measurement of a Q-switched nanosecond laser pulse by CS-CMUI. (a) Schematic diagram of the generation of a nanosecond laser pulse with E-shaped modulation for measurement. (b),(c) Representative reconstructed intensity and phase images of the E-shaped laser pulse. (d) Integrated intensity over time from (b) (green line), associated with the pulse intensity evolution of 1D measurements by streak camera (orange line) and its Gaussian fitting (magenta line). (e) Phase gradient over time at the orange and magenta crosshair positions in (c).
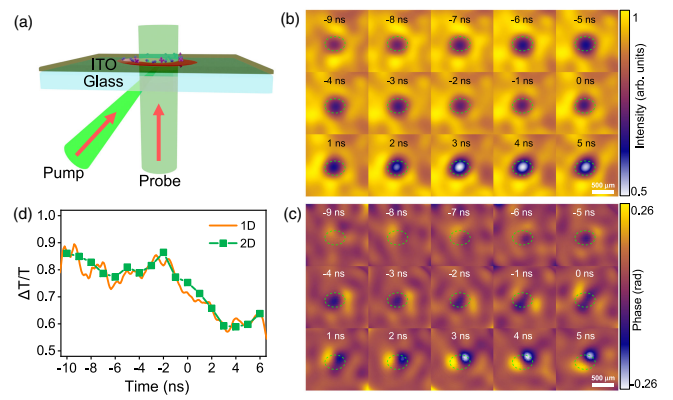

FIG. 5. Real-time detection of an ITO film laser ablation by CS-CMUI. (a) Schematic diagram of ITO laser ablation. (b), (c) Spatiotemporal intensity and phase evolutions during ITO ablation process, the green dashed circles indicate the relative aperture size after ablation. (d) Relative transmittance $\Delta T/T$ (green dotted line) calculated from the 2D intensity images in (b), associated with the corresponding result of 1D measurement by a streak camera (orange line).

camera in 1D dynamic mode, and the measured result is also depicted in Fig. 4(d), together with a Gaussian fitting. Obviously, the calculated laser pulse intensities do not fully exhibit a Gaussian distribution, but almost fall within the direct 1D measurement results, because there is a periodic fluctuation in the intensity. As shown in Fig. 4(c), the spatial phase distribution shows a consistent concave tendency, which coincides with the physical property of the rear cavity mirror in Q-switched laser. The phase gradients at the two points labeled by the orange and magenta crosshairs in the first frame of Fig. 4(c) are calculated using a first order differencing, as shown in Fig. 4(e). It can be observed that, when the laser cavity curvature stays unchanged, the phase gradient remains constant. However, there is an obvious phase gradient change at the time zero, which may be due to the thermal lensing phenomenon caused by the high pulse peak intensity [37].

Furthermore, the laser ablation dynamics on an ITO thin film is investigated by CS-CMUI. As illustrated in Fig. 5(a), a nanosecond pump laser pulse is obliquely irradiated onto the ITO film's surface, and the laser induced ablation dynamics is detected using another nanosecond probe laser pulse perpendicular to the surface, which are further elaborated in Supplemental Material, Note 6 [22]. Based on our experimental measurement and image reconstruction, 17 intensity and 17 phase images of the measured laser pulse are recovered to show the ablation process induced by the second pump laser pulse, and the selected intensity and phase images from −9 to 5 ns are, respectively, depicted in Figs. 5(b) and 5(c), where the time zero is corresponding to maximum pump laser

pulse intensity. The complete sequence is available in Supplemental Material, Movie 2 [22].

Compared to directly analyzing the intensity images in Fig. 5(b), the relative transmittance $\Delta T/T$ can provide a more intuitive parameter for understanding the laser ablation dynamics, where ΔT and T represent the transmitted probe laser pulse intensities with and without passing through the ablation region, respectively [38]. Therefore, the average relative transmittance $\Delta T/T$ in each intensity image of Fig. 5(b) is calculated, and the result is shown in Fig. 5(d), together with the direct measurement result by using the streak camera in 1D dynamic mode. It is evident that the 2D calculated result is highly consistent with the 1D measurement result. Initially, the relative transmittance $\Delta T/T$ remains constant at approximately 0.86 due to the irradiation of the first pump laser pulse. Once the ablation occurs by the second pump laser pulse, the relative transmittance $\Delta T/T$ exhibits a slight decrease followed by an obvious increase to nearly 0.87. Subsequently, the relative transmittance $\Delta T/T$ rapidly decreases to approximately 0.58, which persists for the next few tens of nanoseconds. This evolution behavior is in agreement with the previous studies based on the expansion and diffusion model [36]. As shown in Fig. 5(c), before the ablation occurrence induced by the second pump laser pulse, the phase distribution almost stays unchanged. With the increase of the instantaneous intensity within the pump laser pulse, the phase value in the ablation region begins to decrease. An abrupt phase change is observed at the time of about −2 ns, and then this region expands with a drop in the phase value. This observation corresponds to the sudden increase in the relative transmittance $\Delta T/T$ at the same time, which can be attributed to the plasma formation and expansion [39]. Within the observation time window, the

maximum phase difference caused by laser ablation can reach 0.516 radians. This capability for high-resolution quantitative phase detection yields pivotal data for examining the material transformation processes.

In this Letter, a novel technique called CS-CMUI is introduced, which integrates multiple technical methods, including compressive imaging, coherent modulation imaging, and streak imaging. Meanwhile, a highly efficient image reconstruction algorithm is designed for CS-CMUI, which combines deep learning with traditional iterative algorithms. Through numerical simulation and experimental measurements, we confirm that CS-CMUI allows for the quantitative detection of the complex amplitude information for the ultrafast events with a single measurement, involving both the intensity and phase information. Despite the excellent performance of CS-CMUI, there is still room for improvement in terms of imaging speed, imaging quality, and imaging dimensions [40–43]. With further development, CS-CMUI is poised to become the preeminent single-shot ultrafast imaging method, which will be highly applicable in various fields of ultrafast optical imaging, especially in the occasion of high-resolution ultrafast phase imaging.

---

[*]These authors contributed equally to this work.
[†]dlqi@lps.ecnu.edu.cn
[‡]jqzhu@siom.ac.cn
[§]sazhang@phy.ecnu.edu.cn

[1] H. Mikami, L. Gao, and K. Goda, Nanophotonics **5**, 497 (2016).

[2] J. Liang and L. V. Wang, Optica **5**, 1113 (2018).

[3] D. Qi, S. Zhang, C. Yang, Y. He, F. Cao, J. Yao, P. Ding, L. Gao, T. Jia, and J. Liang, Adv. Opt. Photonics **2**, 014003 (2020).

[4] M. Spellauge, C. Doñate-Buendía, S. Barcikowski, B. Gökce, and H. P. Huber, Light Sci. Appl. **11**, 68 (2022).

[5] N. Zhang, X. Zhu, J. Yang, X. Wang, and M. Wang, Phys. Rev. Lett. **99**, 167602 (2007).

[6] Y. Zhang, B. Shen, T. Wu, J. Zhao, J. C. Jing, P. Wang, K. Sasaki-Capela, W. G. Dunphy, D. Garrett, and K. Maslov, Nat. Commun. **13**, 5247 (2022).

[7] J. Liang, C. Ma, L. Zhu, Y. Chen, L. Gao, and L. V. Wang, Sci. Adv. **3**, e1601814 (2017).

[8] C. Yang, F. Cao, D. Qi, Y. He, P. Ding, J. Yao, T. Jia, Z. Sun, and S. Zhang, Phys. Rev. Lett. **124**, 023902 (2020).

[9] C. F. D. Faria and A. S. Maxwell, Rep. Prog. Phys. **83**, 034401 (2020).

[10] T. L. Nguyen, S. Pradeep, R. L. Judson-Torres, J. Reed, M. A. Teitell, and T. A. Zangle, ACS Nano **16**, 11516 (2022).

[11] J. Moon, S. Yoon, Y.-S. Lim, and W. Choi, Opt. Express **28**, 4463 (2020).

[12] H. Tang, T. Men, X. Liu, Y. Hu, J. Su, Y. Zuo, P. Li, J. Liang, M. C. Downer, and Z. Li, Light Sci. Appl. **11**, 244 (2022).

[13] C. Hu, Z. Du, M. Chen, S. Yang, and H. Chen, Opt. Lett. **44**, 4419 (2019).

[14] Y. Xu, X. Pan, M. Sun, W. Liu, C. Liu, and J. Zhu, Photonics Res. **10**, 1937 (2022).

[15] M. Elad, Sparse and Redundant Representations: From Theory to Applications in Signal and Image Processing (Springer, New York, 2010), Vol. 2.

[16] R. Kodama, K. Okada, and Y. Kato, Rev. Sci. Instrum. **70**, 625 (1999).

[17] F. Zhang, B. Chen, G. R. Morrison, J. Vila-Comamala, M. Guizar-Sicairos, and I. K. Robinson, Nat. Commun. **7**, 13367 (2016).

[18] S. Chan, X. Wang, and O. Elgendy, IEEE Trans. Comput. Imaging **3**, 84 (2017).

[19] D. Ulyanov, A. Vedaldi, and V. Lempitsky, in Proceedings of the IEEE Conference on Computer Vision and Pattern Recognition (IEEE, Salt Lake City, 2018), pp. 9446–9454.

[20] Z. Sun, F. Latorre, T. Sanchez, and V. Cevher, in Proceedings of the 2021 IEEE International Conference on Acoustics, Speech and Signal Processing (ICASSP) (IEEE, Toronto, 2021), pp. 8103–8107.

[21] S. Boyd, N. Parikh, E. Chu, B. Peleato, and J. Eckstein, Found. Trends® Mach. Learn. **3**, 1 (2011).

[22] See Supplemental Material at http://link.aps.org/supplemental/10.1103/PhysRevLett.132.173801 for details on the mathematical principle, the data simulation, the experiment methods, and the movies, which includes Refs. [23–35].

[23] S. V. Venkatakrishnan, C. A. Bouman, and B. Wohlberg, in 2013 IEEE Global Conference on Signal and Information Processing (IEEE, Austin, 2013), pp. 945–948.

[24] Z. Kong, F. Deng, H. Zhuang, X. Yang, J. Yu, and L. He, arXiv:2304.08990.

[25] X. Wang, F. Yu, Z.-Y. Dou, T. Darrell, and J. E. Gonzalez, in Proceedings of the European Conference on Computer Vision (ECCV) (Springer, Munich, 2018), pp. 409–424.

[26] K. Zhang, W. Zuo, and L. Zhang, IEEE Trans. Comput. Imaging **27**, 4608 (2018).

[27] P. Lalanne, S. Astilean, P. Chavel, E. Cambril, and H. Launois, J. Opt. Soc. Am. A **16**, 1143 (1999).

[28] P. Wang, J. Liang, and L. V. Wang, Nat. Commun. **11**, 2091 (2020).

[29] Hamamatsu, Guide to Streak Cameras (2008), https://www.hamamatsu.com/content/dam/hamamatsu-photonics/sites/documents/99_SALES_LIBRARY/sys/SHSS0006E_STREAK.pdf.

[30] K. Liu, S. Sun, A. Majumdar, and V. J. Sorger, Sci. Rep. **6**, 37419 (2016).

[31] M. Grishin, J. Opt. Soc. Am. B **28**, 433 (2011).

[32] B. E. Saleh and M. C. Teich, Fundamentals of Photonics (John Wiley & Sons, New York, 2019).

[33] Changchun New Industries Optoelectronics Technology Co., Ltd., Data Sheet of DPS-532-A, http://www.cnilaser.com/PDF/DPS-532-A.pdf.

[34] M. Cann, M. J. Large, S. J. Henley, D. Milne, T. Sato, H. Chan, I. Jurewicz, and A. B. Dalton, Mater. Today Commun. **7**, 42 (2016).

[35] A. Thøgersen, M. Rein, E. Monakhov, J. Mayandi, and S. Diplas, J. Appl. Phys. **109**, 113532 (2011).

[36] G. E. Hallum, D. Kürschner, D. Redka, D. Niethammer, W. Schulz, and H. P. Huber, Opt. Express **29**, 30062 (2021).

[37] M. Wohlmuth, C. Pflaum, K. Altmann, M. Paster, and C. Hahn, Opt. Express **17**, 17303 (2009).

[38] R. Pohl, C. W. Visser, G.-W. Römer, D. Lohse, C. Sun, and B. Huisint Veld, Phys. Rev. Appl. **3**, 024001 (2015).

[39] J. Wu, W. Wei, X. Li, S. Jia, and A. Qiu, Appl. Phys. Lett. **102**, 164104 (2013).

[40] P. Wang and L. V. Wang, Adv. Sci. **10**, 2207222 (2023).

[41] C. Yang, D. Qi, F. Cao, Y. He, J. Yao, P. Ding, X. Ouyang, Y. Yu, T. Jia, S. Xu, Z. Sun, and S. Zhang, Phys. Rev. Appl. **13**, 024001 (2020).

[42] J. Liang, J. Cao, G. Sun, K. Zhang, L. Van Gool, and R. Timofte, in *Proceedings of the IEEE/CVF International Conference on Computer Vision* (IEEE, Montreal, 2021), pp. 1833–1844.

[43] P. Ding, Y. Yao, D. Qi, C. Yang, F. Cao, Y. He, J. Yao, C. Jin, Z. Huang, L. Deng, L. Deng, T. Jia, J. Liang, Z. Sun, and S. Zhang, Adv. Opt. Photonics **3**, 045001 (2021).